for all the time points. Mean AP did not differ statistically between VX and VS groups. Mean AP in the VSP group progressively decreased and became significantly lower than the VX group after 15 min of the ischemic period. Mean AP in the VSP group was also significantly lower than the VS group after 45 min of the ischemic period.

Discussion

We have shown that electrical vagal stimulation suppressed ischemia-induced NE release and enhanced an initial increase in the ACh levels in the ischemic myocardium. Fixed-rate pacing abolished the suppression of ischemia-induced NE release by vagal stimulation in the present experimental settings.

Effects of vagal stimulation on ischemia-induced NE release

Several mechanisms can be put forward to explain the suppression of ischemia-induced myocardial interstitial NE release by vagal stimulation. First, activation of presynaptic muscarinic receptors on the sympathetic nerve endings inhibits the exocytotic NE release under normal physiological conditions (Levy and Blattberg, 1976). However, the presynaptic inhibition is unlikely the mechanism underlying the vagally mediated suppression of the ischemia-induced NE release because of the following reasons. Although the exocytotic release mechanism participates in the ischemia-induced NE release within the first 20 min of ischemia, the non-exocytotic release mechanism becomes predominant as the ischemic period is prolonged (Akiyama and Yamazaki, 1999). Myocardial ischemia gradually depletes ATP in the ischemic region including sympathetic nerve terminals, which leads to accumulation of axoplasmic NE and reduction of normal Na^+gradient across the plasma membrane in the sympathetic nerve terminals. The NE uptake transporter on the sympathetic nerve terminals, driven by the Na^+gradient, is then reversed, evoking non-exocytotic NE release (Schwartz, 2000). Therefore, the presynaptic inhibition of exocytotic NE release might contribute little to the suppression of ischemia-induced NE release during prolonged ischemia. Furthermore, the presynaptic inhibition of exocytotic NE release becomes less effective during the ischemic insult (Du et al., 1990; Haunstetter et al., 1994). The fact that the ischemia-induced NE release did not differ between the VSP and VX groups is also in opposition to the presynaptic inhibition as a chief mechanism underlying the vagally mediated suppression of ischemia-induced NE release (Fig. 1). Although left ventricular pacing could have affected myocardial interstitial NE levels, the results of the supplemental protocol indicates that changes in the NE levels by ventricular pacing might be negligibly small compared to the ischemia-induced NE release.

Second, the suppression of ischemia-induced NE release by vagal stimulation may be related to myocardial protection via direct vasodiation of the coronary artery. The coronary dilation may enhance collateral flow in the ischemic region and protect against myocardial deterioration evoked by ischemia. Both ACh and vasoactive intestinal polypeptide (VIP) are known to exert direct coronary dilation (Feliciano and Henning, 1998; Gross et al., 1981; Henning and Sawmiller, 2001). VIP is colocalized with ACh in the postganglionic vagal fibers and is released by high-frequency (20 Hz) vagal stimulation. VIP may interact with NE transport or exocytosis like nociceptin (Yamazaki et al., 2001). However, fixed-rate pacing abolished the ability of vagal stimulation to suppress the ischemia-induced NE release. Hence the direct coronary vasodilation and/or interaction with the sympathetic system via VIP might have played little role in suppressing ischemia-induced NE release in the present experimental settings. Another factor that should be taken into account is that the relatively low-frequency (5 Hz) stimulation might have limited the amount of VIP release from the vagal nerve endings.

Third, HR is one of the most important determinants of myocardial oxygen consumption (Mohrman and Heller, 1997). In the present study, HR in the VS group decreased to approximately 60% that of the VX group during the ischemic period (Fig. 3), which slowed the energy consumption of the myocardium. Bradycardia might also decrease ventricular contractility via a force-frequency mechanism (Maughan et al., 1985). In addition, bradycardia may increase coronary perfusion via prolongation of diastolic interval (Buck et al., 1981). These factors slowed energy consumption in the ischemic region including sympathetic nerve terminals, delaying the time course for non-exocytotic NE release. The prevention of excess NE would further reduce myocardial oxygen consumption and decelerate the progression of ischemic injury (Suga et al., 1983). The ischemia-induced NE release did not differ between the VSP and VX groups despite the lower mean AP in the VSP compared with the VX group. Although lowering AP might decrease afterload of the ventricle and reduce energy consumption, the beneficial effect of afterload reduction might have been masked in the VSP group due to inefficient cardiac pumping function associated with asynchrony between sinus rate and ventricular rate. Proper atrioventricular conduction time contributes to the ventricular filling (Meisner et al., 1985). In the VSP group, the sinus rate was reduced by vagal stimulation whereas the ventricular rate was maintained by fixed-rate pacing. Dissociation of the sinus rate and ventricular rate might have impaired the ventricular filling to a variable extent, resulting in a progressive reduction in AP.

Finally, the vagal stimulation decreases ventricular contractile force against sympathetic activation via the direct projections to the ventricle (Nakayama et al., 2001). This mechanism might have also contributed to the reduction of the myocardial oxygen consumption and slowed the progression of ischemic injury in the VS group. However, the ventricular pacing canceled the protective effects in the VSP group, possibly by the adverse influences discussed in the previous paragraph. Further studies are required to isolate the factor(s) most important for the suppression of ischemia-induced NE release by the vagal stimulation.

Effects of vagal stimulation on ischemia-induced ACh release

In contrast to the suppressive effect of NE release, vagal nerve stimulation can exert two opposing influences on ACh release in the ischemic myocardium. The nerve stimulation itself induces exocytotic ACh release from nerve endings. Acute myocardial ischemia impairs conduction of the nerves traversing in the ischemic region (Barber et al., 1983; Inoue and Zipes, 1988; Martins et al., 1989). Acute myocardial ischemia also impairs the exocytotic ACh release in the postischemic myocardium (Kawada et al., 2002b). On the other hand, acute myocardial ischemia causes myocardial ACh release in the ischemic region via a local release mechanism independent of efferent nerve activity (Kawada et al., 2000). Hence, the amount of ACh release was net effects of ACh release evoked by nerve stimulation and ischemia; vagally mediated protection against ischemic injury should augment the former and attenuate the latter.

Although vagal stimulation augmented myocardial interstitial ACh release during the 0–15 min period of coronary occlusion in the VS group than in the VX group, the initial enhancement was not observed in the VSP group. One possible mechanism for the difference in the initial ACh release between the VS and VSP groups is that the progression of ischemia in the VSP group relative to the VS group impaired the vagal nerve conduction in the ischemic region, reducing the exocytotic ACh release. The other possible mechanism is that the high levels of NE might have attenuated the stimulation-induced ACh release from the vagal nerve endings via α-adrenergic mechanisms (Akiyama and Yamazaki, 2000).

There are several limitations to the present study. First, we avoided large myocardial ischemia by occluding LAD just distal to the first diagonal branch. Accordingly, the incidence of lethal ventricular arrhythmia was too low to draw any conclusion as to the effects of vagal stimulation on the arrhythmogenesis. Further studies with larger myocardial ischemia are clearly required to examine the effects of vagal stimulation on the incidence of lethal ventricular arrhythmia in relation to the observed NE and/or ACh levels in the ischemic myocardium. Second, plasma catecolamine levels might have been increased during the LAD occlusion, which might affect HR and cardiac function in the non-ischemic region. Although changes in plasma catecholamine levels may play significant roles in determining systemic hemodynamics, the ischemic region was only poorly perfused. Accordingly, direct effects of plasma catecholamines on the myocardial interstitial NE and ACh levels in the ischemic region might have been limited in the present study.

Conclusion

Electrical vagal stimulation suppressed ischemia-induced NE release in the ischemic myocardium in anesthetized cats. The vagal stimulation augmented ischemia-induced ACh release at the 0–15 min period of ischemia. Although acute myocardial ischemia causes myocardial NE and ACh releases independent of efferent nerve activity, the vagal stimulation was able to modulate both NE and ACh levels in the ischemic region. The suppression of NE release and augmentation of initial ACh release in the ischemic myocardium by vagal stimulation may reduce the ischemic injury to the heart. The direct neural intervention could be a new modality of medical engineering to cope with ischemic heart diseases.

Acknowledgments

This study was supported by Health and Labour Sciences Research Grant for Research on Advanced Medical Technology (H14-Nano-002) from the Ministry of Health Labour and Welfare of Japan, by Grant-in-Aid for Scientific Research (C-15590786) from the Ministry of Education, Science, Sports and Culture of Japan, and by the Program for Promotion of Fundamental Studies in Health Science from the Organization for Pharmaceutical Safety and Research.

References

Akiyama, T., Yamazaki, T., 1999. Norepinephrine release from cardiac sympathetic nerve endings in the in vivo ischemic region. Journal of Cardiovascular Pharmacology 34, S11–S14.

Akiyama, T., Yamazaki, T., 2000. Adrenergic inhibition of endogenous acetylcholine release on postganglionic cardiac vagal nerve terminals. Cardiovascular Research 46, 531–538.

Akiyama, T., Yamazaki, T., Ninomiya, I., 1991. In vivo monitoring of myocardial interstitial norepinephrine by dialysis technique. American Journal of Physiology. Heart and Circulatory Physiology 261, H1643–H1647.

Akiyama, T., Yamazaki, T., Ninomiya, I., 1994. In vivo detection of endogenous acetylcholine release in cat ventricles. American Journal of Physiology. Heart and Circulatory Physiology 266, H854–H860.

Armour, J.A., 1999. Myocardial ischaemia and the cardiac nervous system. Cardiovascular Research 41, 41–54.

Barber, M.J., Mueller, T.M., Henry, D.P., Felten, S.Y., Zipes, D.P., 1983. Transmural myocardial infarction in the dog produces sympathectomy in noninfarcted myocardium. Circulation 67, 787–796.

Buck, J.D., Warltier, D.C., Hardman, H.F., Gross, G.J., 1981. Effects of sotalol and vagal stimulation on ischemic myocardial blood flow distribution in the canine heart. Journal of Pharmacological and Experimental Therapeutics 216, 347–351.

Du, X.J., Dart, A.M., Riemersma, R.A., Oliver, M.F., 1990. Failure of the cholinergic modulation of norepinephrine release during acute myocardial ischemia in the rat. Circulation Research 66, 950–956.

Feliciano, L., Henning, R.J., 1998. Vagal nerve stimulation releases vasoactive intestinal peptide which significantly increases coronary artery blood flow. Cardiovascular Research 40, 45–55.

Glantz, S.A., 2002. Primer of Biostatistics, 5th ed. McGraw-Hill, New York.

Gross, G.J., Buck, J.D., Warltier, D.C., 1981. Transmural distribution of blood flow during activation of coronary muscarinic receptors. American Journal of Physiology. Heart and Circulatory Physiology 240, H941–H946.

Haunstetter, A., Haass, M., Yi, X., Krüger, C., Kübler, W., 1994. Muscarinic inhibition of cardiac norepinephrine and neuropeptide Y release during ischemia and reperfusion. American Journal of Physiology. Regulatory, Integrative and Comparative Physiology 267, R1552–R1558.

Henning, R.J., Sawmiller, D.R., 2001. Vasoactive intestinal peptide: cardiovascular effects. Cardiovascular Research 49, 27–37.

Inoue, H., Zipes, D.P., 1988. Time course of denervation of efferent sympathetic and vagal nerves after occlusion of the coronary artery in the canine heart. Circulation Research 62, 1111–1120.

Kawada, T., Yamazaki, T., Akiyama, T., Sato, T., Shishido, T., Inagaki, M., Takaki, H., Sugimachi, M., Sunagawa, K., 2000. Differential acetylcholine release mechanisms in the ischemic and non-ischemic myocardium. Journal of Molecular and Cellular Cardiology 32, 405–414.

Kawada, T., Yamazaki, T., Akiyama, T., Inagaki, M., Shishido, T., Zheng, C., Yanagiya, Y., Sugimachi, M., Sunagawa, K., 2001. Vagosympathetic interactions in ischemia-induced myocardial norepinephrine and acetylcholine release. American Journal of Physiology. Heart and Circulatory Physiology 280, H216–H221.

Kawada, T., Yamazaki, T., Akiyama, T., Mori, H., Inagaki, M., Shishido, T., Takaki, H., Sugimachi, M., Sunagawa, K., 2002. Effects of brief ischaemia on myocardial acetylcholine and noradrenaline levels in anaesthetized cats. Autonomic Neuroscience 95, 37–42.

Kawada, T., Yamazaki, T., Akiyama, T., Mori, H., Uemura, K., Miyamoto, T., Sugimachi, M., Sunagawa, K., 2002. Disruption of vagal efferent axon and nerve terminal function in the postischemic myocardium. American Journal of Physiology. Heart and Circulatory Physiology 283, H2687–H2691.

Lameris, T.W., de Zeeuw, Sandra, Alberts, G., Boomsma, F., Duncker, D.J., Verdouw, P.D., Veld, A.J., van den Meiracker, A.H., 2000. Time course and mechanism of myocardial catecholamine release during transient ischemia in vivo. Circulation 101, 2645–2650.

Levy, M.N., Blattberg, B., 1976. Effect of vagal stimulation on the overflow of norepinephrine into the coronary sinus during cardiac sympathetic nerve stimulation in the dog. Circulation Research 38, 81–84.

Li, M., Zheng, C., Sato, T., Kawada, T., Sugimachi, M., Sunagawa, K., 2004. Vagal nerve stimulation markedly improves long-term survival after chronic heart failure in rats. Circulation 109, 120–124.

Martins, J.B., Lewis, R., Wendt, D., Lund, D.D., Schmid, P.G., 1989. Subendocardial infarction produces epicardial parasympathetic denervation in canine left ventricle. American Journal of Physiology. Heart and Circulatory Physiology 256, H859–H866.

Maughan, W.L., Sunagawa, K., Burkhoff, D., Graves, W.L. Jr., Hunter, W.C., Sagawa, K., 1985. Effect of heart rate on the canine end-systolic pressure–volume relationship. Circulation 72, 654–659.

Meisner, J.S., McQueen, D.M., Ishida, Y., Vetter, H.O., Bortolotti, U., Strom, J.A., Frater, R.W.M., Peskin, C.S., Yellin, E.L., 1985. Effects of timing of atrial systole on LV filling and mitral valve closure: computer and dog studies. American Journal of Physiology. Heart and Circulatory Physiology 249, H604–H619.

Mohrman, D.E., Heller, L.J., 1997. Cardiovascular Physiology, 4th ed. McGraw-Hill, New York, pp. 47–69.

Nakayama, Y., Miyano, H., Shishido, T., Inagaki, M., Kawada, T., Sugimachi, M., Sunagawa, K., 2001. Heart rate-independent vagal effect on end-systolic elastance of the canine left ventricule under various levels of sympathetic tone. Circulation 104, 2277–2279.

Przyklenk, K., Kloner, R.A., 1995. Low-dose i.v. acetylcholine acts as a "preconditioning-mimetic" in the canine model. Journal of Cardiac Surgery 10, 389–395.

Rosenshtraukh, L., Danilo Jr., P., Anyukhovsky, E.P., Steinberg, S.F., Rybin, V., Brittain-Valenti, K., Molina-Viamonte, V., Rosen, M.R., 1994. Mechanisms for vagal modulation of ventricular repolarization and of coronary occlusion-induced lethal arrhythmias in cats. Circulation Research 75, 722–732.

Schömig, A., Fischer, S., Kurz, T., Richardt, G., Schömig, E., 1987. Nonexocytotic release of endogenous noradrenaline in the ischemic and anoxic rat heart: mechanism and metabolic requirements. Circulation Research 60, 194–205.

Schwartz, J.H., 2000. Neurotransmitters. In: Kandel, E.R., Schwartz, J.H., Jessell, T.M. (Eds.), Principles of Neural Science, 4th ed. McGraw-Hill, New York, pp. 280–297.

Snedecor, G.W., Cochran, W.G., 1989. Statistical Methods, 8th ed. Iowa State, Iowa, pp. 290–291.

Suga, H., Hisano, R., Goto, Y., Yamada, O., Igarashi, Y., 1983. Effect of positive inotropic agents on the relation between oxygen consumption and systolic pressure volume area in canine left ventricle. Circulation Research 53, 306–318.

Vanoli, E., De Ferrari, G.M., Stramba-Badiale, M., Hull Jr., S.S., Foreman, R.D., Schwartz, P.J., 1991. Vagal stimulation and prevention of sudden death in conscious dogs with a healed myocardial infarction. Circulation Research 68, 1471–1481.

Yamazaki, T., Akiyama, T., Kitagawa, H., Takauchi, Y., Kawada, T., Sunagawa, K., 1997. A new, concise dialysis approach to assessment of cardiac sympathetic nerve terminal abnormalities. American Journal of Physiology. Heart and Circulatory Physiology 272, H1182–H1187.

Yamazaki, T., Akiyama, T., Mori, H., 2001. Effects of nociceptin on cardiac norepinephrine and acetylcholine release evoked by ouabain. Brain Research 904, 153–156.

The EMBO Journal (2006) 25, 2889–2897 | © 2006 European Molecular Biology Organization | All Rights Reserved 0261-4189/06
www.embojournal.org

THE EMBO JOURNAL

Endophilin BAR domain drives membrane curvature by two newly identified structure-based mechanisms

Michitaka Masuda[1,4], Soichi Takeda[2,3,4], Manami Sone[1], Takashi Ohki[1], Hidezo Mori[2], Yuji Kamioka[1] and Naoki Mochizuki[1,*]

[1]Department of Structural Analysis, National Cardiovascular Center Research Institute, Suita, Osaka, Japan, [2]Department of Cardiac Physiology, National Cardiovascular Center Research Institute, Suita, Osaka, Japan and [3]Laboratory of structural biochemistry, RIKEN Harima Institute at SPring-8, Mikazuki-cho, Sayo, Hyogo, Japan

The crescent-shaped BAR (Bin/Amphiphysin/Rvs-homology) domain dimer is a versatile protein module that senses and generates positive membrane curvature. The BAR domain dimer of human endophilin-A1, solved at 3.1 Å, has a unique structure consisting of a pair of helix–loop appendages sprouting out from the crescent. The appendage's short helices form a hydrophobic ridge, which runs across the concave surface at its center. Examining liposome binding and tubulation *in vitro* using purified BAR domain and its mutants indicated that the ridge penetrates into the membrane bilayer and enhances liposome tubulation. BAR domain-expressing cells exhibited marked plasma membrane tubulation *in vivo*. Furthermore, a swinging-arm mutant lost liposome tubulation activity yet retaining liposome binding. These data suggested that the rigid crescent dimer shape is crucial for the tubulation. We here propose that the BAR domain drives membrane curvature by coordinate action of the crescent's scaffold mechanism and the ridge's membrane insertion in addition to membrane binding via amino-terminal amphipathic helix.

The EMBO Journal (2006) **25**, 2889–2897. doi:10.1038/sj.emboj.7601176; Published online 8 June 2006
Subject Categories: membranes & transport; structural biology
Keywords: BAR domain; endophilin; liposome; membrane curvature; membrane insertion

Introduction

Membrane dynamics in a cell, such as membrane budding, tubulation, fission and fusion, is associated with changes in membrane curvature. The crystal structure of amphiphysin BAR (Bin/Amphiphysin/Rvs-homology) domain revealed an unexpected structural identity with arfaptin2, a binding protein to Arf and Rac small GTPases (Tarricone *et al*, 2001), and provided a common structural base for the sensing and the formation of positive curvature membrane by BAR-family proteins (Peter *et al*, 2004).

Endophilins are cytoplasmic proteins containing an N-terminal BAR domain and a C-terminal SH3 domain, and are involved in membrane dynamics (Schuske *et al*, 2003; Galli and Haucke, 2004; Wenk and De Camilli, 2004). There are five endophilin genes in the mammalian genomes, endophilin A1–3 and B1–2. Both A and B types are highly conserved from nematode to human. The most extensively studied one is endophilin-A1, a brain specific protein involved in clathrin-mediated synaptic vesicle endocytosis (Ringstad *et al*, 1997, 2001). Via SH3 domain, endophilins bind to the GTPase dynamin, a membrane scissor, and the polyphosphoinositide phosphatase synaptojanin, a clathrin-uncoater (Ringstad *et al*, 1997; de Heuvel *et al*, 1997; Verstreken *et al*, 2003). The BAR domain of endophilins is classified into the N-BAR subgroup characterized by a short amphipathic helical sequence preceding the consensus BAR-domain sequence (Peter *et al*, 2004). The N-BAR domain of endophilin-A1 binds to liposomes and induces the tubulation *in vitro*, requiring the short amphipathic helical sequence (Farsad *et al*, 2001).

The crescent-shaped BAR dimer structure implies a simple model to drive membrane curvature: the dimer may impress its positively charged concave surface on the negatively charged membrane to form a high-curvature membrane domain (Gallop and McMahon, 2005; McMahon and Gallop, 2005). This curvature-impressing or scaffold mechanism for membrane deformation is based on an assumption that the dimer behaves as a rigid body on the membrane (Zimmerberg and Kozlov, 2006). Although the essential requirement of positively charged residues on the concave surface has been suggested (McMahon and Mills, 2004; Peter *et al*, 2004), there have been no experimental supports for the scaffold mechanism. Here, we show the requirement of the molecular rigidity of the BAR dimer for membrane curvature on the basis of structure-oriented mutational analysis.

By determining the structure of endophilin-A1 BAR domain, we found a distinction from those of the known BAR domains: a helix–loop appendage of 30 amino acids stretch is inserted into the helix I of the canonical BAR domain. A pair of the helices of the appendages forms a hydrophobic ridge, which runs across the center of the concave surface of the dimer. We analyzed the function of this ridge as well as the previously proposed structure, the N-terminal amphipathic helix and the crescent main body, for membrane deformation (Peter *et al*, 2004). N-terminal amphipathic helix is essential for membrane binding. The crescent main body of the BAR dimer is required for impressing its intrinsic curvature to the membrane. The ridge contributes to deform the membrane

*Corresponding author. Department of Structural Analysis, National Cardiovascular Center Research Institute, 5-7-1 Fujishiro-dai, Suita, Osaka 565-8565, Japan. Tel.: +81 6 6833 5012; Fax: +81 6 6835 5461; E-mail: nmochizu@ri.ncvc.go.jp
[4]These authors contributed equally to this work

Received: 15 November 2005; accepted: 8 May 2006; published online: 8 June 2006

presumably by penetrating into the membrane. Our results illustrate how these three components coordinate to induce membrane deformation.

Results

Endophilin-A1 BAR domain has a unique appendage

The structure of the BAR domain of human endophilin-A1 (amino acid 1–247, hereafter EndA1-BAR) was solved at 3.1 Å resolution by a multi-wavelength anomalous dispersion method. The structure of EndA1-BAR dimer is similar to that of amphiphysin (Peter *et al*, 2004) and arfaptin2 (Tarricone *et al*, 2001): a crescent-shaped dimer composed of a 6-helix bundle core and two 3-helix bundle arms extended from the core (Figure 1A). The whole structure of EndA1-BAR dimer can be precisely superimposed on that of amphiphysin and arfaptin (Figure 1B). All three structures show nearly identical dimer shapes. Notably, the present EndA1-BAR structure from a tetragonal crystal packing is almost completely the same as an independent crystal structure from an orthogonal crystal packing (Supplementary Figure 1; and Weissenhorn, 2005). The RMS deviations are 0.63, 0.86 and 0.80 Å for Cα atoms in monomers A, B and dimer, respectively. The structural identity indicates that the crescent shape is stably present in solution. Consistent with previous results (Habermann, 2004; Peter *et al*, 2004), structure-based sequence alignment reveals that these three proteins are poorly conserved in amino-acid sequence including the residues possibly important for the crescent-shape formation (Supplementary Figure 2).

We find a unique structure of the EndA1-BAR, an appendage-like structure protruded from the center of the dimer (Figure 1A). The sequence alignments of the BAR-family proteins indicated that this appendage appears unique to the endophilin-family proteins including nadrin (Habermann, 2004; Peter *et al*, 2004) and the candidates from yeasts (Supplementary Figure 2). The appendage (Q59–Q88) has an N-terminal short helix and a loop of which electron density is mostly missing (N72–G85). The pair of helices appears to stay on the main body and forms a ridge across the center of the concave dimer surface. The helix displays, on its top surface, a series of hydrophobic residues (P62, A63, A66 and M70) aligned 60° against the longitudinal axis of the dimer (Figure 1C). Other than the conserved hydrophobic amino acids of the ridge, the appendage sequences show clear distinction between endophilin-A and endophilin-B (Supplementary Figure 2). The B type endophilins show cytoplasmic localization, presumably being involved in intracellular membrane dynamics (Farsad *et al*, 2001; Modregger *et al*, 2003; Karbowski *et al*, 2004). Analyses of chimeric mutations in the appendage between EndA1-BAR and EndB1-BAR suggest that BAR domain may contribute to defining where to target, plasma membrane or intracellular organ membrane (Supplementary Figure 3).

The appendage's penetration enhances liposome tubulation

To investigate the functional significance of the hydrophobic ridge of the endophilin-specific appendage, we first examined the effects of point mutations in this region (red residues in Figure 1C) on the liposome binding and tubulation activities *in vitro* (Figures 2A and 3). Introduction of membrane-repulsive negative charge (A66D) lost the ability to form tubes from liposomes. Hydrophilic mutations (A63S/A66S (SS) and A63S/A66S/M70Q (SSQ)) reduced the number of tubes (<1/100) and induced three-time enlargement of the tube diameter. In contrast, a bulky hydrophobic residue

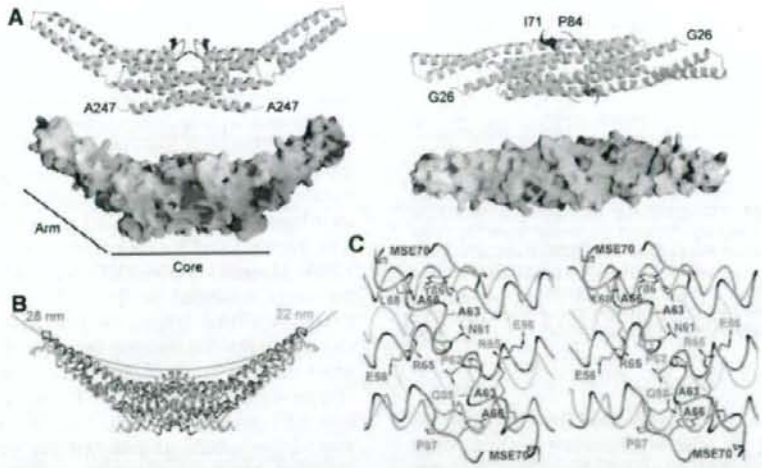

Figure 1 Structure of human endophilin-A1 BAR domain dimer. (**A**) Ribbon representation (a green monomer with a red appendage and a pale-blue monomer with a blue appendage) and surface electrostatic potential (red, $-15\,kTe^{-1}$; blue, $15\,kTe^{-1}$) of the dimer viewed from the side (left) and from the top (right). The numbered amino-acid residues are the first and the last ones in consecutive polypeptide segments determined in this model. (**B**) Comparison of three BAR domain structures in trace representation. Red, endophilin-A1 (PDB ID: 1X03); green, amphiphysin (1URU); blue, arfaptin2 (1I4D). The red and green arcs with indicated diameters represent curved membranes fit the concave surface of endophilin-A1 and amphiphysin, respectively. (**C**) Stereo view of the appendages. Side-chains of the residues forming the hydrophobic ridge and those of interacting with residues of the main body are shown.

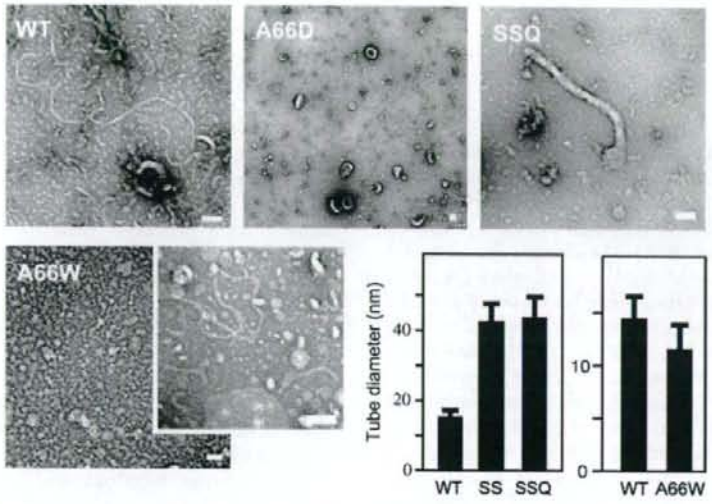

Figure 2 Liposome tubulation by endophilin-A1 BAR domains with mutations in the hydrophobic ridge. WT, 7 μM wild-type BAR domain incubated for 10 min; A66D, 28 μM, 10 min; SSQ, A63S/A66S/M70Q triple mutant, 28 μM, 10 min; A66W, 1.4 μM, 10 min (vesiculated, left panel) and 10 s (tubulated, right panel). Tubulation was not observed when incubated for longer than 1 min. Scale, 100 nm. The bar graphs show tubule diameter (mean and s.d.). SS, A63S/A66S double mutant, 28 μM, 10 min.

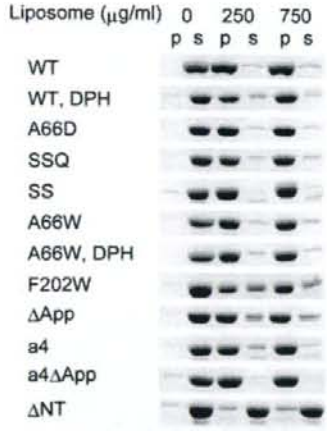

Figure 3 Liposome binding assays of endophilin-A1 BAR domain and its mutants. Protein (200 μg/ml) was co-sedimented with liposomes (0, 250 and 750 μg/ml). Proteins recovered from the pellet (p) and the supernatant (s) were analyzed by SDS-PAGE. The DPH-liposomes show similar binding capacity for the wild type (WT) and the A66W mutants. The liposome binding activity is slightly reduced in the F202W and the appendage-less mutants (ΔApp) and is almost lost in the helix 0 truncated mutant (ΔNT).

(A66W) led to extensive vesiculation and less tubulation. All these mutations did not affect the liposome binding. These results suggest an important role for the hydrophobic ridge in the membrane curvature formation but not in the membrane binding.

Although the ridge reduces the intrinsic curvature of the concave surface (red line in Figure 1B), it appears to promote the membrane curvature formation with conserved hydrophobicity. This raises the possibility that the ridge penetrates into the membrane when the concave surface makes tight contact with the membrane. This possibility was investigated using tryptophan fluorescence, which is sensitive to hydrophobicity of the microenvironment around the indole moiety. The A66W mutant showed 10-nm blueshift of the fluorescence peak in a liposome-dose-dependent and saturable manner, while F202W, a control mutant in which Phe202 on the convex surface was mutated to Trp, did not show any shift (Figure 4A and Supplementary Figure 5). The amount of the blueshift was greater than that observed in 50% DMSO or 50% methanol, indicating that the indol moiety was in a highly hydrophobic environment.

To determine whether this blueshift was caused by the insertion of the indol moiety into the hydrophobic core of the lipid bilayer, we made fluorescence resonance energy transfer (FRET) assays using diphenyl-hexatriene (DPH) as the acceptor probe. DPH has been shown to insert specifically in the nonpolar interior of the membrane and not to alter the membrane structure and dynamics (Repáková *et al*, 2005). DPH liposomes did not affect liposome binding and tubulation (Figure 3 and Supplementary Figure 4). A66W but not F202W showed effective FRET from the 340-nm tryptophan fluorescence (donar) to the DPH fluorescence (acceptor) peaked at 430 nm (Figure 4B and C). It was not caused by changes in the fluorescence property of DPH itself possibly accompanied by tubulation/vesiculation of liposomes (Figure 4D and Supplementary Figure 6). These data suggest that the indol ring of 66W penetrates into the hydrophobic core of the membrane and that the remaining residues of the ridge, about 8 Å in height, appear to be embedded in the layer of lipid head-groups of the contacting membrane leaflet. These results confirmed that the ridge is contacting membrane and that the convex is not contacting membrane surface.

To provide further support for the membrane insertion of the ridge in the wild-type EndA1-BAR, we made a mutant

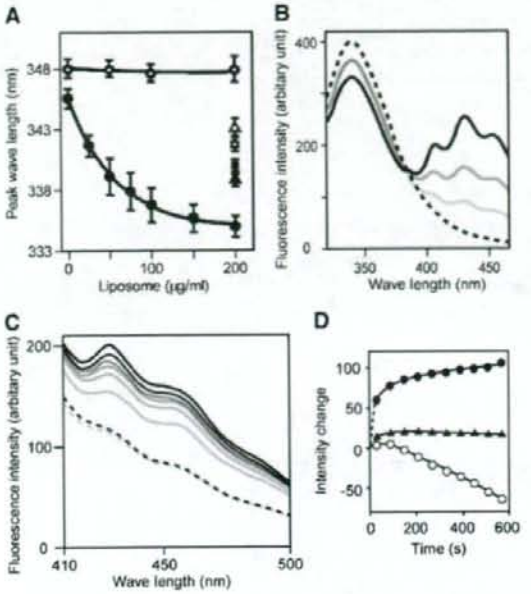

Figure 4 Tryptophan fluorescence blueshift and FRET assays. (**A**) Tryptophan fluorescence emission peak when excited at 280 nm was observed in different concentration of liposome. A66W (●), F202W control mutant (○), A66W alone in 50% DMSO (▲), in 50% MeOH (■), F202W alone in 50% DMSO (△), in 50% MeOH (□), 140 μg/ml protein for all measurements. Mean and s.d. ($N=4$–11). The dose dependency is significant ($P \ll 0.001$) for the A66W mutant but insignificant ($P > 0.8$) for the F202W mutant (one-way ANOVA). DMSO and MeOH were used as blueshift inducer for tryptophan. (**B**) Dose-dependent FRET efficiency from the A66W tryptophan to DPH incorporated in liposomes was examined by the changes of fluorescence. Fluorescence spectrum of A66W (100 μg/ml) with the control liposome (200 μg/ml) excited at 280 nm (hatched). Pale to dark solid curves represent DPH:lipid weight ratios of 1:2000, 1:1000 and 1:500 in the same condition. (**C**) Time-dependent increase in the FRET efficiency from either A66W (pale to dark solid lines, from 30 to 570 s) or F202W tryptophan (pale and dark hatched lines, at 30 and 570 s) to DPH incorporated in liposomes. DPH:lipid weight ratio is 1:500. (**D**) The intensity changes at the 430-nm peak are plotted against time. A66W (●), F202W (▲) excited at 280 nm and A66W (○) excited at 360 nm.

with amphiphysin/arfaptin shape and examined its tubulation activity. The mutant (ΔApp), in which the entire appendage (Q59–Q88) was replaced with a helical stretch (AHLSSLLQ) derived from arfaptin2 sequence (A152–Q159, Y155S), show the crystal structure of a canonical BAR-domain dimer as designed (Figure 5A and Supplementary Figure 7). The ΔApp could bind to liposomes (Figure 3) and cause tubulation to a lesser extent than the wild type and amphiphysin-BAR (Figure 5D and Supplementary Figure 4). As the diameter of the tubules reflects the membrane curvature if the section of the tube is circle, we measured the diameter of the tube to compare the curvature of the EndA1-BAR and its mutant-induced tubes. Despite the higher curvature of the concave surface, the ΔApp dimer induced larger diameter tubules than the wild type did, indicating a positive contribution of the wild-type hydrophobic ridge to drive membrane curvature. Taken all together, the hydrophobic ridge penetrates into the interfacial leaflet of the lipid bilayer when the concave surface is in contact with the membrane and promotes membrane curvature formation.

The BAR domain is rigid enough to impose its intrinsic curvature on membrane

A simple model for the concave surface-driven mechanism is that each BAR domain dimer acts as a molecular mold that impresses its curved surface on the membrane. This model suggests that the membrane curvature approximately mirrors the curvature of the concave surface. Indeed, the diameters of tubules induced by amphiphysin, ΔApp (Figure 5D), SS and SSQ mutants (Figure 2) are compatible with the model-based prediction (see Supplementary Table II for statistical analysis). However, this model has an assumption that the dimer should be rigid enough to overcome the bending resistance of the membrane (Nossal and Zimmerberg, 2002; Farsad and De Camilli, 2003). To examine whether the molecular mold mechanism is feasible, we developed a straight BAR domain by inserting one helical pitch into the helix II in the proximal portion of the extending arm (QSAL is inserted between I154 and Q155). This mutation (a4) would compensate the unequal lengths between helix II and III in the arm, a common feature of the known BAR domain structures, and let the curved arm into a straight one. Although the a4 mutant was designed simply to straighten the curvature of the domain, the structure solved at 2.4 Å resolution shows that it actually has the very interesting property of a flexible arm rather than a rigid one (Figure 5B). Four monomers in the asymmetrical unit show deviation in the bending angles of arms. The blue and the green monomers have straight arms while the orange monomer shows a bending pattern similar to the wild type and the yellow monomer is an intermediate. The structural deviation almost exclusively occurs in the helix kink regions (Supplementary Figure 8), indicating that the arm can swing at least from the bend-free straight position to nearly the wild-type position.

The a4 mutant allowed us to examine how flexibility of the crescent-shaped main body of the BAR dimer affects the membrane curvature formation. The insertion of one helical pitch slightly distorts relative position of the helix II and III (Figure 5C), but does not largely rearrange the spatial positions of the residues on the concave surface of the arm (Supplementary Figure 8). Indeed, the a4 mutant and its appendage-lacking derivative (a4ΔApp) retained normal liposome binding activity (Figure 3). The a4 mutant vesiculated liposomes without any tubulation, while a4ΔApp lost these membrane-deforming activities (Figure 5D and Supplementary Figure 4). The concave surface-induced membrane deforming activity appeared to be lost in the a4 mutant, while the appendage's membrane insertion remained active. These results suggested that the rigidity of the crescent dimer structure is essential for liposome tubulation but not for vesiculation, although appendage insertion induces the vesiclulation.

Roles for the amphipathic helix 0 of the N-BAR domain

The structure of a short amphipathic helix (helix 0) characterizing the N-BAR (Peter *et al*, 2004) can be resolved in the a4 mutant structure due to its tight crystal packing (Figures 5B and 6). The helix 0 is disordered in the wild type (Figure 6) and the ΔApp structures. The helix 0 has been

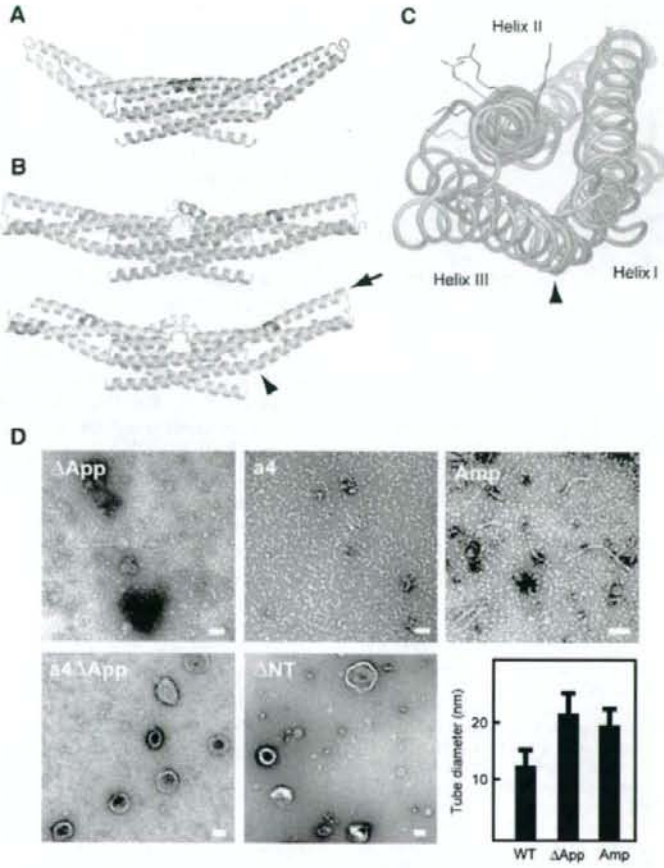

Figure 5 Distinct liposome tubulation induced by endophilin-A1 BAR domain mutants. (**A**) Ribbon representation of a mutated EndA1-BAR dimer lacking the entire appendages (ΔApp, PDB ID: 1X04). The entire appendage (Q59–Q88) was replaced with a helical stretch (AHLSSLLQ) derived from arfaptin2 sequence (A152–Q159, Y155S). Red, mutated segment. (**B**) Ribbon representation of the a4 mutant with swinging arms (PDB ID: 2D4C). One helical pitch was inserted into the helix II in the proximal portion of the extending arm (QSAL was inserted between I154 and Q155). Two dimers in the asymmetrical unit are shown separately. Red, inserted segment; magenta, helix 0. The bending patterns of the helix II and III varies among four monomers. An obvious kink in the helix III remains in the orange monomer (arrowhead, also in (C)). The residual curvature in the blue–green dimer is provided by the intersection of the monomers. (**C**) Superimposition of the a4 mutant monomer (orange one in (B)) and the wild-type monomer (blue) in the core region. A view from the distal end along the helix II (arrow in (B)) shows the maximum structural difference in these arms. Side chains of K171, 173 and R174 are shown. The helix III rotates 12° counterclockwise and shift 6 Å relative to the helix II at the distal end of the arm. The helix 0 and the core region are omitted. (**D**) Negatively stained liposome tubules induced by the BAR domains of endophilin mutants and amphiphysin. ΔApp, 7 μM, incubated for 10 min; a4, 7 μM, 10 min; a4ΔApp, 28 μM, 10 min; ΔNT, 21 μM, 10 min; Amp, 7 μM, 10 min. Note that a4, a4ΔApp, and ΔNT do not induce liposome tubulation. Scale, 100 nm. The bar graph shows tubule diameter (mean and s.d.).

suggested to be helical only when the amphiphysin BAR domain binds to liposomes (Peter *et al*, 2004). The helix 0 displays the hydrophobic branch of T14, V17 and V21 on one side, while K12, K16 and E19 on the other side (Figure 6). The helix 0 is connecting with the Helix I by a flexible linker G23–G24–A25. Consistent with the previous report (Farsad *et al*, 2001), truncation of the helix 0 (ΔNT) resulted in loss of liposome binding activity (Figure 3) and consequently abolished the tubulation (Figure 5D). In contrast, all the helix 0-containing mutants, including the A66D and the a4ΔApp showed intact liposome binding activity irrespective of their tubulation or vesiculation activities. These results indicate that the helix 0 in the endA1-BAR is critical for liposome binding and that the membrane binding of endA1-BAR via helix 0 is not sufficient to induce tubulation or vesiculation.

BAR domain induces tubular membrane deformation in vivo

To explore the significance of the helix 0, the rigid crescent mold, and the appendage of endophilin-A1 BAR domain *in vivo*, we further examined the membrane deformation activity of endophilin-A1 BAR domain in cells (Figure 7). Human umbirical vascular endothelial cells (HUVECs) expressing endophilin-A1 lacking SH3 domain (residues 1–296, hereafter, EndA1-BAR296), which was C-terminally tagged with enhanced green fluorescence protein (EGFP), exhibited intracellular fibrous structure similar to those induced by other BAR domain-containing molecules (Kamioka *et al*, 2004; Itoh *et al*, 2005). Notably, these structures developed from the periphery toward the center of the cells dynamically and disappeared reversibly in living cells (Figure 7E and

Supplementary Movie 1). Furthermore, these GFP-marked structures were co-localized with *in vivo* biotin-labeled membrane (Figure 7D), indicating that EndA1-BAR296-induced fibrous structure seems to be a membrane invagination originated from the plasma membrane. These structures were found in other cells we tested (Figure 7C). In clear contrast, ΔApp, ΔNT and a4 were incapable of inducing membrane deformation in cells, indicating the importance of helix 0, the rigid crescent shape, and the appendage of BAR domain for membrane deformation *in vivo*.

Discussion

The endophilin-A1 BAR domain dimer consists of three sub-modules: the crescent-shaped main body, the helix 0 and the unique appendage. We tried to understand the functional roles for these sub-modules in the membrane curvature formation. In this study by determining the structure of endopholin-A1 BAR domain and developing mutants that were critical for the sub-module structure, we have explored the roles of sub-modules.

Here, we show that the structural rigidity of the crescent-shaped main body is critical for membrane tubulation. The BAR dimer is sufficiently rigid to overcome the bending resistance of the membrane and to be scaffolds for the tubulation (McMahon and Gallop, 2005; Zimmerberg and Kozlov, 2006). The insertion of one helical-pitch into the helix II at distal to the kink brings flexibility to the dimer (a4 mutant). The relative position of the three helices in the

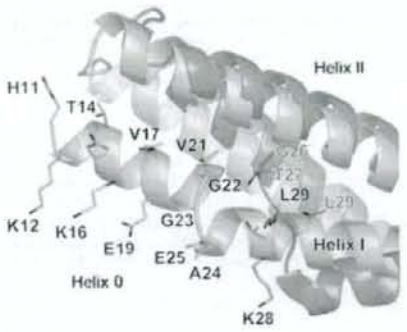

Figure 6 Close-up of helix 0 in an a4 mutant monomer (orange). The same superimposition as in Figure 5C but viewed from the side and displays the helix 0. The helix 0 is disordered in the wild-type structure (blue). The side chains of N-terminal residues are shown (H11KATQKVSEKVGGAEGTKL29 in the a4 and G26TKL in the wild type). The amphipathic helix 0 is stabilized by hydrophobic interactions with the helix II and III and also by hydrogen bonds with a symmetrical molecule.

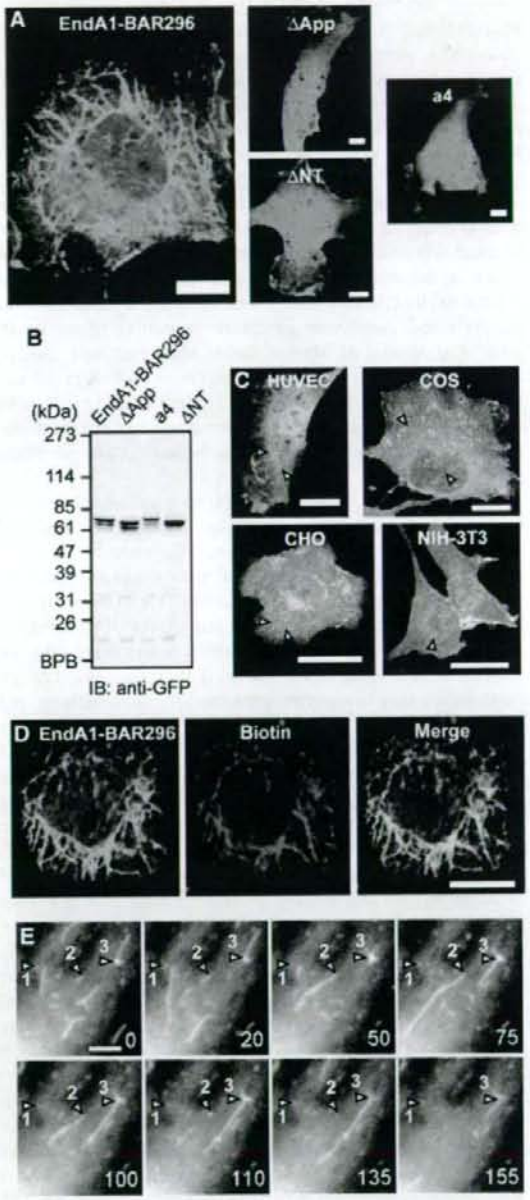

Figure 7 Endophilin A1 BAR domain induces membrane tubulation *in vivo*. (**A**) HUVECs were transfected with plasmids expressing C-teminally EGFP-tagged EndA1-BAR296 (amino acid 1–296 of endophilin-A1), ΔApp, a4, and ΔNT. Cells were GFP-imaged on an epifluorescnce microscope (Olympus IX-71). Fibrous structures were observed exclusively in EndA1-BAR296-expressing cells. Scale, 10 μm. (**B**) Protein expression of the EndA1-BAR296 and the mutants tagged with EGFP in transfected 293T cells were examined by immunoblotted with anti-GFP antibody. (**C**) Cells indicated were similarly transfected to (A). Arrowheads indicate the fibrous structures. Scale, 20 μm. (**D**) Live HUVECs expressing EGFP-tagged EndA1-BAR296 were biotinylated with sulfo-NHS-biotin for 10 min and chased for further 10 min. Covalently bound biotin was visualized using Alexa633-streptavidine. Fluorescnece images for EGFP (left), Alexa633 (center), and merge (right) are shown. Scale, 10 μm. (**E**) A time lapse images of HUVECs expressing EGFP-tagged EndA1-BAR296 were obtained at the time point (seconds) after the observation (Supplementary Movie 1). EGFP-marked structure grows from the cell periphery towards the center of the cell. Notably, both extension and retraction of GFP-marked structure is observed (numbered arrow heads indicate each extending/retracting structure). Scale, 5 μm.

mutant arm was not changed in a4 mutant irrespective of the bend levels (Supplementary Figure 8). The mutant arm behaves as a rigid body and its structure changes only in the vicinity of the helix kinks when it swings. Therefore, it is unlikely that the flexibility of the mutant dimer can be a result of weakened inter-helix interactions in the arm. Moreover, we could not find any specific structural features in the kink region that might explain the flexible hinge in the swinging-arm mutant as well as the rigid bend in the wild-type BAR dimers of endophilin, amphiphysin, and arfaptin.

In this study, for the first time we could determine the structure of the N-terminal amphipathic helix (helix 0) using a swinging-arm mutant. Our mutant and previous mutation analyses indicated that the N-terminal helical sequence of endophilin-A1 is indispensable for liposome binding (Farsad *et al*, 2001), whereas that of amphiphysin is important but not essential for liposome binding and tubulation (Peter *et al*, 2004). The BAR domain of endophilin-A1 is an acidic polypeptide and the cluster of positive charge at the distal end of the arm is not prominent (Figure 1A). This property can explain the critical role for the helix 0 of the EndA1-BAR in liposome binding by providing additional basic residues. The helix 0 structure suggests that K12, K16 and possibly K8 are in a suitable position for cooperation with the positive charge cluster at the distal end. The amphipathic nature of the helix 0 implies that it can also insert into the membrane and facilitate the membrane curvature formation (Peter *et al*, 2004; Gallop and McMahon, 2005; McMahon and Gallop, 2005). Loss of the membrane-deforming activities of the A66D mutant (Figure 2) and the a4ΔApp mutant (Figure 5D) accounts for the additional mechanism for membrane deformation in addition to the membrane insertion of the helix 0.

The N-BAR of endophilins has one additional step to tubulate membrane. Here, we show that the hydrophobic ridge of the endophilin-specific appendage is inserted into the contacting membrane surface. Our data suggested that the entire ridge of the wild-type BAR domain, about 8 Å in height, is embedded in the layer of lipid head-groups of the contacting membrane leaflet. The embedding of the ridge into the membrane is consistent with the local spontaneous curvature mechanism that is reported very recently (Zimmerberg and Kozlov, 2006). As a protruding structure found in epsin1 induces liposome tubulation by being inserted to one leaflet of the lipid bilayer (Ford *et al*, 2002), the penetration of the hydrophobic ridge can drive the positive curvature by causing asymmetrical expansion of the surface area between two leaflets as shown in Figure 8 (Farsad and De Camilli, 2003).

We further explored the importance of the ridge, rigid crescent shape, and helix 0 in cells. We for the first time showed that N-BAR domain induced membrane invaginations originated from plasma membrane, although other BAR-containing molecules have been reported to induce similar invaginations (Itoh *et al*, 2005). Neither mutant that lacked either the ridge or the helix 0 nor flexible mutant formed the tubular invaginations in cells, indicating the significance of these sub-module structure in cells as suggest by *in vitro* studies. We constructed a series of endorphin-A1-EGFP expression plasmids to delineate the domain for the membrane invagination. Full-length endophilin-expressing cells did not show any tubular formation. Because endophilin consists of BAR domain and an SH domain, SH3-binding molecule such as dynamin may inhibit the extension of membrane invagination. This possibility has been suggested in the membrane invagination found in FBP17 and amphiphysin (Kamioka *et al*, 2004; Itoh *et al*, 2005).

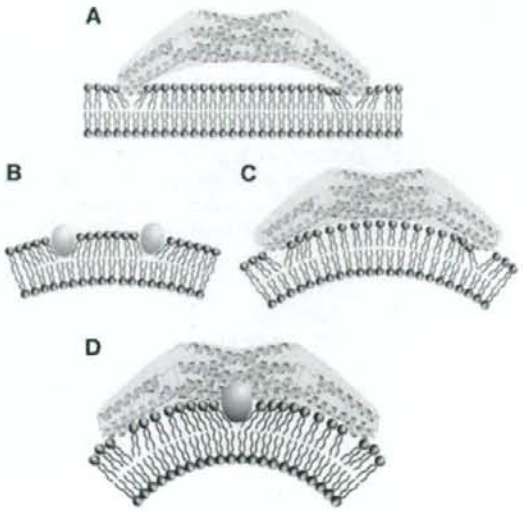

Figure 8 Two potential mechanisms for driving membrane curvature by endophilin-A1. (**A**) Kissing adhesion of an N-BAR domain on planar lipid bilayer. The helix 0 is essential for the membrane binding. Membrane insertion of the helix 0 is supposed. (**B**) Insertion of hydrophobic portions of macromolocules into one leaflet can create bilayer surface discrepancy that causes membrane curvature. (**C**) The simple N-BAR domain, such as amphiphysin and ΔApp, induces membrane curvature by impressing the concave surface onto the membrane. The rigidity of the molecule is required for this mechanism. (**D**) To drive membrane curvature, the endophilin N-BAR domain uses both the rigid crescent shape-mediated deformation and the insertion of hydrophobic ridge on the concave surface in addition to kissing adhesion of N-BAR to membrane surface.

Collectively, EndA1-BAR uses two newly identified mechanisms to drive positive membrane curvature in addition to the essential binding capacity of helix 0 to the membrane: one by the scaffold mechanism common to the BAR domains and the other by the local spontaneous curvature mechanism caused by the membrane insertion of the ridge (Figure 8D). The ridge, which occupies the bottom of the concave lipid-binding surface, may not work until the main body of the BAR dimer localizes itself to a curved membrane. The ridge then inserts into the bilayer roughly perpendicular to the main body, and thus both deformations will occur in the same direction.

Materials and methods

Protein expression and purification by CRECLE

cDNAs encoding BAR domains (amphiphysin1, 1–239; endophilin-A1, 1–247; endophilin-B1, 1–246 in amino-acid residues) were amplified by PCR from a human brain cDNA library. Recombinant proteins were expressed in *Escherichia coli* as GST-fusions using the pGEX6p3 vector, purified by glutathione-Sepharose, cleaved from the GST-tag using Prescission protease (Amersham Biosciences), and further purified by ion-exchange chromatography (Yamagishi *et al*, 2004). The final polypeptide contained an artificial linker

sequence of GPLGS at the N-terminus. EndA1-BAR proteins except for F202W and a4 mutants were purified by crystallization during Prescission protease cleavage. The method, crystallization by regulated cleavage of large hydrophilic tag (CRECLE), was as follows. Purified GST fusions were concentrated to 20–30 mg/ml in an elution buffer (20 mM glutathione, 100 mM Tris–HCl, pH 8.0, 10 mM DTT, 1 mM EDTA, 1 mM EGTA) and then cleaved by a low concentration of prescission protease (1 U/mg protein or less) at 4°C. Slow increase in the tag-free protein concentration might be suitable for crystallization and more than a half of EndA1-BAR protein could be recovered as 20–100 μm microcrystals. They were washed with a low-salt buffer (20 mM HEPES, pH 7.4, 2 mM DTT, 0.2 mM EDTA, 0.2 mM EDTA) and resolved into a high-salt buffer (350 mM NaCl in the low-salt buffer) and used for further analyses.

Protein crystallization

Seleno-methionine (S-Met) derivatives of the EndA1-BAR domain and its appendage-less mutant (ΔApp) were produced in B834(DE3)pLysS cells using Overnight Express Autoinduction System 2 (Novagen). To make X-ray grade crystals in a cryo-ready condition, modified high salt buffer (50 mM HEPES, pH 7.4, 300 mM NaCl, 100 mM KI, 28% ethylene glycol, 5% glycerol, 25 mM DTT) was used. Crystals of 1 mm size were formed by dialysis against 50 mM CHES, pH 9.5, 260 mM NaCl, 28% ethylene glycol, 5% glycerol, 25 mM DTT, 0.4% benzamidine·HCl at 4°C and were flush frozen at 100 K. Crystals could also be grown by vapor diffusion from a similar protein solution using distilled water as the bath solution. The crystals were equilibrated in 50 mM HEPES, pH 7.4, 150 mM NaCl, 25 mM DTT, 0.4% benzamidine·HCl, 5% PEG 8000 and the saturated amount of xylitol as a cryoprotectant. Some of the crystals were soaked with 0.5 mM oleoyl-L-α-lysophosphatidic acid (Sigma) or malonyl-CoA (Sigma) for 4 days with daily change for the substrates. The a4 mutant crystals were grown by sitting-drop vapour diffusion using a bath solution containing 100 mM HEPES, pH 7.2, 200 mM calcium acetate, 10 mM DTT and 20% (w/v) PEG3350 at 20°C and then flush frozen after brief immersion in the same solution containing 16% DMSO. The wild type and the ΔApp mutant crystals belong to the same space group $I4_1$ and contain one monomer molecule in the asymmetric unit (Supplemental Figure 1). The a4 crystal belongs to $P2_1$ and contains two dimers in the asymmetric unit.

Structural determination

The EndA1-BAR structure was determined using the multiple anomalous dispersion (MAD) method. Multiple-wavelength X-ray diffraction data sets were collected from a single Se-Met crystal (crystal I) at SPring-8 beamline BL44B2 (Supplementary Table I). Single wavelength data sets of another crystal (crystal II) and of a ΔApp crystal used for the refinement were collected at BL45PX. The data set for the a4 mutant was collected at BL38B1. All diffraction data sets were collected at 90 K and were processed using HKL2000 suite (Otwinowski and Minor, 1997). The seven positions out of 10 expected selenium atoms were identified by SOLVE (Terwilliger and Berendzen, 1999). The initial phases calculated by SOLVE with a figure of merit of 0.59 at 3.2 Å resolution were further improved by RESOLVE (Terwilliger, 1999). The density modified MAD map (Supplementary Figure 1) had sufficient quality to trace the polypeptide chain except for the N-terminus and the loop region of the appendage. The model was built with TURBO-FRODO (Roussel and Cambillau, 1996) and refined to the resolutions of 3.1 Å by CNS (Brunger *et al*, 1998). The final model includes 210 residues (residues 26–71 and 84–247), and has an R factor of 23.6% (R_{free} of 26.4%). The ΔApp structure was solved by molecular replacement by MOLREP in the CCP4 suite (CCP4, 1994) and refined to the resolution of 2.9 Å by CNS. The simulated annealing omit electron density map calculated by CNS confirmed the continuous α-helical structure of the replaced region as designed (Supplementary Figure 7). The final model includes 200 amino-acid residues and has an R factor of 23.8% (R_{free} of 26.9%). The a4 mutant structure was solved by molecular replacement using the central core of the EndA1-BAR as a starting model and the arms were manually built (Supplementary Figure 7). The structure was refined to the resolution of 2.4 Å by CNS with an R factor of 21.5% (R_{free} of 26.9%). Main-chain dihedral angles of all non-glycine residues of these three models lie in allowed regions of the Ramachandran plot, with 94.3% for the EndA1-BAR, 94.1% for the ΔApp mutant, and 96.4% for the a4 mutant in most-favored regions, respectively. Graphical representations were prepared using the programs TURBO-FRODO, MOLSCRIPT (Kraulis, 1991), RASTER3D (Merritt and Bacon, 1997), GRASP (Nicholls *et al*, 1991) and Pymol (DeLano, 2002).

Liposome binding and tubulation assays

Liposome sedimentation assay and tubulation assay were as earlier described (Peter *et al*, 2004 see also McMahon lab protocols: http://www2.mrc-lmb.cam.ac.uk/NB/McMahon_H/group/techniqs/techniqs.htm) with slight modifications. Briefly, Folch fraction 1 (Sigma) was used as the lipid source and liposome suspension, 1 mg/ml in liposome buffer (20 mM HEPES, pH 7.4, 150 mM NaCl, 1 mM DTT) was made by sonication. Freshly purified BAR domain proteins were diluted at about 1 mg/ml in the liposome buffer and ultracentrifuged at 400 000 *g* for 10 min just before use. No crystallization occurred at this or lower concentrations. For sedimentation assays, 20 μg proteins were mixed with 25 or 75 μg liposomes in 100 μl of the liposome buffer, incubated for 10 min on ice and ultracentrifuged at 200 000 *g* for 10 min. For tubulation assays, 400 μg/ml proteins were mixed with an equal volume of 400 μg/ml liposomes, left for 10 s to 30 min at room temperature, and then processed for negative staining. Judging from the liposome sedimentation and the tryptophan fluorescence assays, this protein to lipid ratio ensured nearly saturated protein–liposome binding. Magnification was calibrated using a grating replica of 2160/mm.

Tryptophan fluorescence and FRET assay

Fluorescence emission spectra were recorded with a Hitachi F-4500 fluorescence spectrophotometer (Ohki *et al*, 2004). For tryptophan fluorescence assays, 140 μg/ml tryptophan-containing mutants were mixed with 0–200 μg/ml liposomes in the liposome buffer, incubated for 3 min, and excited at 280 nm. For FRET assays, DPH-liposomes were made by adding DPH (Molecular Probe) into lipid solution (1:500 to lipid, w:w). The fluorescence of DPH-liposomes (200 μg/ml) excited at 280 nm was scanned from 400 to 500 nm at 1-min intervals. The first measurement of the 430-nm DPH peak was obtained at about 30 s after mixing with mutant proteins (100 μg/ml).

Cell culture, transfection and surface biotinylation

HUVECs were purchased from Kurabo and cultured in HuMedia-EG2 as described previously (Sakurai *et al*., 2006). 293T cells, CHO cells, Cos7 cells, and NIH-3T3 cells were cultured in DMEM supplemented with 10% fetal bovine serum as described previously (Kamioka *et al*., 2004). Cells were transfected using LipofectAMINE 2000 (Invitrogen). Live HUVECs were biotinylated with 5 mM sulfo-NHS-biotin (Pierce) in Opti-MEM (Invitrogen) for 10 min. They were washed once with Opti-MEM and chased for 10 min with the normal culture medium, and fixed with 2% formaldehyde after a brief wash with Opti-MEM containing 1/20 volume of Avidin D blocking solution (Vector Laboratory) to reduce the cell surface background staining. HUVECs were permeabilized with cold MeOH and biotin was visualized using Alexa633-streptavidine (Molecular Probe).

Supplementary data

Supplementary data are available at *The EMBO Journal* Online.

Acknowledgements

We thank H Nakajima, T Matsu, Y Kawano and H Naitow for technical assistance with SPring-8 beamlines, and H Ago and M Miyano, Structural Biophysics Laboratory, RIKEN Harima Institute at SPring-8, for their helpful advice. This work was supported in part by Grant for Research on Advanced Medical Technology from the Ministry of Health, Labour, and Welfare of Japan, by the Program for Promotion of Fundamental Studies in Health Sciences of the National Institute of Biomedical Innovation (NIBIO), and by Special Coordination Funds for Promoting Science and Technology, Ministry of Education, Culture, Sports, Science and Technology (MEXT) of Japan.

Competing interests statement

The authors declare that they have no competing commercial interests in relation to this work.

References

Brunger AT, Adams PD, Clore GM, DeLano WL, Gros P, Grosse-Kunstleve RW, Jiang JS, Kuszewski J, Nilges M, Pannu NS, Read RJ, Rice LM, Simonson T, Warren GL (1998) Crystallography & NMR system: a new software suite for macromolecular structure determination. *Acta Crystallogr D* **54:** 905–921

Collaborative Computational Project Number 4 (1994) The CCP4 suite: programs for protein crystallography. *Acta Crystallogr D* **50:** 760–763

DeLano WL (2002) *The PyMOL User's Manual*. DeLano Scientific: San Carlos, CA, USA

Galli T, Haucke V (2004) Cycling of synaptic vesicles: How far? How fast!. *Sci STKE* **2004:** re19

Farsad K, Ringstad N, Takei K, Floyd SR, Rose K, De Camilli P (2001) Generation of high curvature membranes mediated by direct endophilin bilayer interactions. *J Cell Biol* **155:** 193–200

Farsad K, De Camilli P (2003) Mechanisms of membrane deformation. *Curr Opin Cell Biol* **15:** 372–381

Ford MG, Mills IG, Peter BJ, Vallis Y, Praefcke GJ, Evans PR, McMahon HT (2002) Curvature of clathrin-coated pits driven by epsin. *Nature* **419:** 361–366

Gallop JL, McMahon HT (2005) BAR domains and membrane curvature: bringing your curves to the BAR. *Biochem Soc Symp* **72:** 223–231

Habermann B. (2004) The BAR-domain family of proteins: a case of bending and binding. *EMBO Rep* **5:** 250–255

de Heuvel E, Bell AW, Ramjaun AR, Wong K, Sossin WS, McPherson PS (1997) Identification of the major synaptojanin-binding proteins in brain. *J Biol Chem* **272:** 8710–8716

Itoh T, Erdmann KS, Roux A, Habermann B, Werner H, De Camilli P (2005) Dynamin and the actin cytoskeleton cooperatively regulate plasma membrane invagination by BAR and F-BAR proteins. *Dev Cell* **9:** 791–804

Kamioka Y, Fukuhara S, Sawa H, Nagashima K, Masuda M, Matsuda M, Mochizuki N. (2004) A novel dynamin-associating molecule, formin-binding protein 17, induces tubular membrane invaginations and participates in endocytosis. *J Biol Chem* **279:** 40091–40099

Karbowski M, Jeong SY, Youle RJ (2004) Endophilin B1 is required for the maintenance of mitochondrial morphology. *J Cell Biol* **166:** 1027–1039

Kraulis PJ (1991) MOLSCRIPT: a program to produce both detailed and schematic plots of protein structure. *J Appl Crystallogr* **24:** 946–950

McMahon HT, Mills IG (2004) COP and clathrin-coated vesicle budding: different pathways, common approaches. *Curr Opin Cell Biol* **16:** 379–391

McMahon HT, Gallop JL (2005) Membrane curvature and mechanisms of dynamic cell membrane remodeling. *Nature* **438:** 590–596

Merritt EA, Bacon DJ (1997) Raster3D: photorealistic molecular graphics. *Methods Enzymol* **277:** 505–524

Modregger J, Schmidt AA, Ritter B, Huttner WB, Plomann M (2003) Characterization of Endophilin B1b, a brain-specific membrane-associated lysophosphatidic acid acyl transferase with properties distinct from endophilin A1. *J Biol Chem* **278:** 4160–4167

Nicholls A, Sharp K, Honig B (1991) Protein folding and association: insights from the interfacial and thermodynamic properties of hydrocarbons. *Proteins* **11:** 281–296

Nossal R, Zimmerberg J (2002) Endocytosis: curvature to the ENTH degree. *Curr Biol* **12:** R770–R772

Ohki T, Mikhailenko SV, Morales MF, Onishi H, Mochizuki N (2004) Transmission of force and displacement within the myosin molecule. *Biochemistry* **43:** 13707–13714

Otwinowski Z, Minor W (1997) Processing of X-ray diffraction data collected in oscillation mode. *Methods Enzymol* **276:** 307–326

Peter BJ, Kent HM, Mills IG, Vallis Y, Butler PJ, Evans PR, McMahon HT (2004) BAR domains as sensors of membrane curvature: the amphiphysin BAR structure. *Science* **303:** 495–499

Repáková J, Holopainen JM, Morrow MR, McDonald MC, Capkova P, Vattulainen I (2005) Influence of DPH on the structure and dynamics of a DPPC bilayer. *Biophys J* **88:** 3398–3410

Ringstad N, Nemoto Y, De Camilli P (1997) The SH3p4/Sh3p8/SH3p13 protein family: binding partners for synaptojanin and dynamin via a Grb2-like Src homology 3 domain. *Proc Natl Acad Sci USA* **94:** 8569–8574

Ringstad N, Nemoto Y, De Camilli P (2001) Differential expression of endophilin 1 and 2 dimers at central nervous system synapses. *J Biol Chem* **276:** 40424–40430

Roussel A, Cambillau C (1996) *TURBO-FRODO Manual*. Marseille France AFMB-CNRS, Paris, France

Sakurai A, Fukuhara S, Yamagishi A, Sako K, Kamioka Y, Masuda M, Nakaoka Y, Mochizuki N (2006) MAGI-1 is required for Rap1 activation upon cell–cell contact and for enhancement of vascular endothelial cadherin-mediated cell adhesion. *Mol Biol Cell* **17:** 966–976

Schuske KR, Richmond JE, Matthies DS, Davis WS, Runz S, Rube DA, van der Bliek AM, Jorgensen EM (2003) Endophilin is required for synaptic vesicle endocytosis by localizing synaptojanin. *Neuron* **40:** 749–762

Tarricone C, Xiao B, Justin N, Walker PA, Rittinger K, Gamblin SJ, Smerdon SJ (2001) The structural basis of Arfaptin-mediated cross-talk between Rac and Arf signalling pathways. *Nature* **411:** 215–219

Terwilliger TC (1999) Reciprocal-space solvent flattening. *Acta Crystallogr D* **55:** 1863–1871

Terwilliger TC, Berendzen J (1999) Automated MAD and MIR structure solution. *Acta Crystallogr D* **55:** 849–861

Verstreken P, Koh TW, Schulze KL, Zhai RG, Hiesinger PR, Zhou Y, Mehta SQ, Cao Y, Roos J, Bellen HJ (2003) Synaptojanin is recruited by endophilin to promote synaptic vesicle uncoating. *Neuron* **40:** 733–748

Weissenhorn W (2005) Crystal structure of the endophilin-A1 BAR domain. *J Mol Biol* **351:** 653–661

Wenk MR, De Camilli P (2004) Protein-lipid interactions and phosphoinositide metabolism in membrane traffic: insights from vesicle recycling in nerve terminals. *Proc Natl Acad Sci USA* **101:** 8262–8269

Yamagishi A, Masuda M, Ohki T, Onishi H, Mochizuki N (2004) A novel actin-bundling/filopodium-forming domain conserved in insulin receptor tyrosine kinase substrate p53 and missing in metastasis protein. *J Biol Chem* **279:** 14929–14936

Zimmerberg J, Kozlov MM (2006) How proteins produce cellular membrane curvature. *Nat Rev Mol Cell Biol* **7:** 9–19

Available online at www.sciencedirect.com
ScienceDirect
Radiation Physics and Chemistry 75 (2006) 1812–1818
Radiation Physics and Chemistry
www.elsevier.com/locate/radphyschem

Preliminary study for producing higher harmonic hard X-rays from weakly ionized nickel plasma

Eiichi Sato[a,*], Yasuomi Hayasi[a], Etsuro Tanaka[b], Hidezo Mori[c], Toshiaki Kawai[d], Takashi Inoue[e], Akira Ogawa[e], Shigehiro Sato[f], Kazuyoshi Takayama[g], Jun Onagawa[h], Hideaki Ido[h]

[a]*Department of Physics, Iwate Medical University, 3-16-1 Honchodori, Morioka 020-0015, Japan*
[b]*Department of Nutritional Science, Faculty of Applied Bio-science, Tokyo University of Agriculture, 1-1-1 Sakuragaoka, Setagaya-ku 156-8502, Japan*
[c]*Department of Cardiac Physiology, National Cardiovascular Center Research Institute, 5-7-1 Fujishirodai, Suita, Osaka 565-8565, Japan*
[d]*Electron Tube Division #2, Hamamatsu Photonics K. K., 314-5 Shimokanzo, Iwata 438-0193, Japan*
[e]*Department of Neurosurgery, School of Medicine, Iwate Medical Universichimaru, Morioka 020-8505, Japan*
[f]*Department of Microbiology, School of Medicine, Iwate Medical University, 19-1 Uchimaru, Morioka 020-8505, Japan*
[g]*Shock Wave Research Center, Institute of Fluid Science, Tohoku University, 2-1-1 Katahira, Sendai 980-8577, Japan*
[h]*Department of Applied Physics and Informatics, Faculty of Engineering, Tohoku Gakuin University, 1-13-1 Chuo, Tagajo 985-8537, Japan*

Accepted 23 November 2005

Abstract

In the plasma flash X-ray generator, a 200 nF condenser is charged up to 50 kV by a power supply, and flash X-rays are produced by the discharging. The X-ray tube is a demountable triode with a trigger electrode, and the turbomolecular pump evacuates air from the tube with a pressure of approximately 1 mPa. Target evaporation leads to the formation of weakly ionized linear plasma, consisting of nickel ions and electrons, around the fine target, and intense Kα lines are left using a 15-μm-thick cobalt filter. At a charging voltage of 50 kV, the maximum tube voltage was almost equal to the charging voltage of the main condenser, and the peak current was about 18 kA. The K-series characteristic X-rays were clean and intense, and higher harmonic X-rays were observed. The X-ray pulse widths were approximately 300 ns, and the time-integrated X-ray intensity had a value of approximately 1.0 mGy at 1.0 m from the X-ray source with a charging voltage of 50 kV.

PACS: 52.80.Vp; 52.90.+z; 87.59.Bh; 87.64.Gb

Keywords: Weakly ionized linear plasma; K-series characteristic X-rays; Clean characteristic X-rays; Higher harmonic hard X-rays

1. Introduction

In conjunction with single crystals, synchrotrons produce monochromatic parallel beams, which are fairly similar to monochromatic parallel laser beams, and the

*Corresponding author.
E-mail address: dresato@iwate-med.ac.jp (E. Sato).

0969-806X/$ - see front matter © 2006 Elsevier Ltd. All rights reserved.
doi:10.1016/j.radphyschem.2005.11.012

beams have been applied to enhanced K-edge angiography (Thompson et al., 1992; Mori et al., 1996; Hyodo et al., 1998), phase-contrast radiography (Davis et al., 1995; Momose et al., 1996; Ando et al., 2002), and crystallography. Therefore, the production of coherent hard X-ray lasers for various research projects, including biomedical applications, has long been wished for.

Recently, soft X-ray lasers have been produced by a gas-discharge capillary (Rocca et al., 1994, 1996; Macchietto et al., 1999), and the laser pulse energy substantially increased in proportion to the capillary length. These kinds of fast discharges can generate hot and dense plasma columns with aspect ratios approaching 1000:1. However, it is difficult to increase the laser photon energy to 10 keV or beyond. Because there are no X-ray resonators in the high-photon-energy region, new methods for increasing coherence will be desired in the future.

To apply flash X-ray generators to biomedicine, several different generators have been developed (Germer, 1979; Sato et al., 1990, 1994a, b; Shikoda et al., 1994; Takahashi et al., 1994), and plasma X-ray generators (Sato et al., 2003a, b, 2004a–c, 2005a–c) are useful for producing clean characteristic X-rays in the low-photon-energy region of less than 20 keV. By forming weakly ionized linear plasma using rod targets, we confirmed irradiation of intense K-series characteristic X-rays from the axial direction of the linear plasmas of nickel, copper, and molybdenum, since the bremsstrahlung X-rays are absorbed effectively by the linear plasma; monochromatic clean Kα rays were produced using K-edge filters.

In this paper, we describe a recent plasma flash X-ray generator utilizing a rod target, used to perform a preliminary experiment for generating clean K-series characteristic X-rays and their higher harmonic hard X-rays by forming a plasma cloud around a fine target.

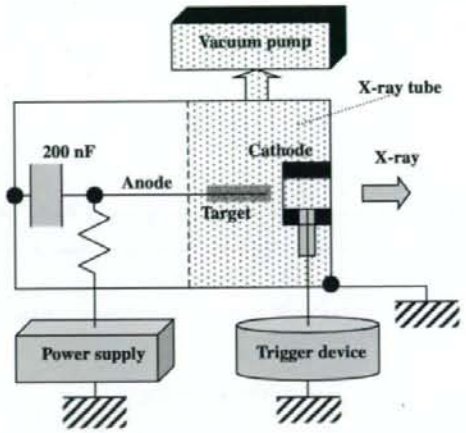

Fig. 1. Block diagram including electric circuit of the plasma flash X-ray generator.

2. Generator

Fig. 1 shows a block diagram of the high-intensity plasma flash X-ray generator. This generator consists of the following essential components: a high-voltage power supply, a high-voltage condenser with a capacity of approximately 200 nF, a turbomolecular pump, a krytron pulse generator as a trigger device, and a flash X-ray tube. The high-voltage main condenser is charged to 50 kV by the power supply, and electric charges in the condenser are discharged to the tube after triggering the cathode electrode with the trigger device. The plasma flash X-rays are then produced.

The schematic drawing of the plasma X-ray tube is illustrated in Fig. 2. The X-ray tube is a demountable

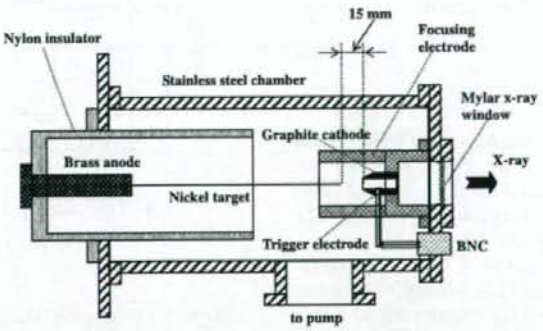

Fig. 2. Schematic drawing of the flash X-ray tube with a rod nickel target.

cold-cathode triode that is connected to the turbomolecular pump with a pressure of approximately 1 mPa. This tube consists of the following major parts: a hollow cylindrical carbon cathode with a bore diameter of 10.0 mm, a brass focusing electrode, a trigger electrode made from copper wire, a stainless steel vacuum chamber, a nylon insulator, a polyethylene terephthalate (Mylar) X-ray window 0.25 mm in thickness, and a rod-shaped nickel target 3.0 mm in diameter with a tip angle of 60°. The distance between the target and cathode electrodes is approximately 15 mm, and the trigger electrode is set in the cathode electrode. As electron beams from the cathode electrode are roughly converged to the target by the focusing electrode, evaporation leads to the formation of a weakly ionized linear plasma, consisting of nickel ions and electrons, around the fine target.

In the linear plasma, bremsstrahlung photons with energies higher than the K-absorption edge are effectively absorbed and are converted into fluorescent X-rays. The plasma then transmits the fluorescent rays easily, and bremsstrahlung rays with energies lower than the K-edge are also absorbed by the plasma. In addition, because bremsstrahlung rays are not emitted in the opposite direction to that of electron trajectory, intense characteristic X-rays are generated from the plasma-axial direction.

3. Characteristics

3.1. Tube voltage and current

Tube voltage and current were measured by a high-voltage divider with an input impedance of 1 GΩ and a current transformer, respectively. Fig. 3 shows the time relation between the tube voltage and current. At the indicated charging voltages, they roughly displayed damped oscillations. When the charging voltage was increased, both the maximum tube voltage and current increased. At a charging voltage of 50 kV, the maximum tube voltage was almost equal to the charging voltage of the main condenser, and the maximum tube current was approximately 18 kA.

3.2. X-ray output

X-ray output pulse was detected using a combination of a plastic scintillator and a photomultiplier (Fig. 4). The X-ray pulse height substantially increased with corresponding increases in the charging voltage. The X-ray pulse widths were about 300 ns, and the time-integrated X-ray intensity measured by a thermoluminescence dosimeter (Kyokko TLD Reader 1500 having MSO-S elements without energy compensation) had a value of about 1.0 mGy at 1.0 m from the X-ray source with a charging voltage of 50 kV.

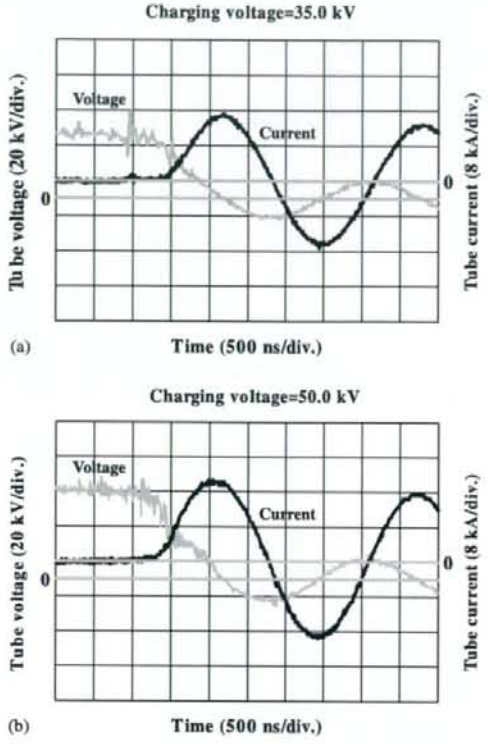

Fig. 3. Tube voltages and currents with a charging voltage of (a) 35.0 kV and (b) 50.0 kV.

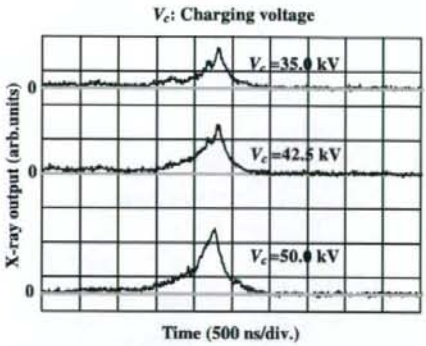

Fig. 4. X-ray outputs at the indicated conditions.

3.3. X-ray source

In order to roughly observe images of the plasma X-ray source in the detector plane, we employed a pinhole camera with a hole diameter of 100 μm (Fig. 5). When

the charging voltage was increased, the plasma X-ray source grew, and both spot dimension and intensity increased. Because the X-ray intensity is the highest at the center of the spot, both the dimension and intensity decreased according to both increases in the thickness of a filter for absorbing X-rays and decreases in the pinhole diameter.

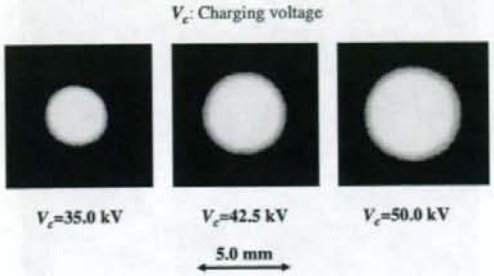

Fig. 5. Images of plasma X-ray source.

3.4. X-ray spectra

X-ray spectra from the plasma source were measured by a transmission-type spectrometer with a lithium fluoride curved crystal 0.5 mm in thickness. The spectra were taken by a computed radiography (CR) system (Sato et al., 2000) (Konica Minolta Regius 150) with a wide dynamic range, and relative X-ray intensity was calculated from Dicom digital data. Subsequently, the relative X-ray intensity as a function of the data was calibrated using a conventional X-ray generator, and we confirmed that the intensity was proportional to the

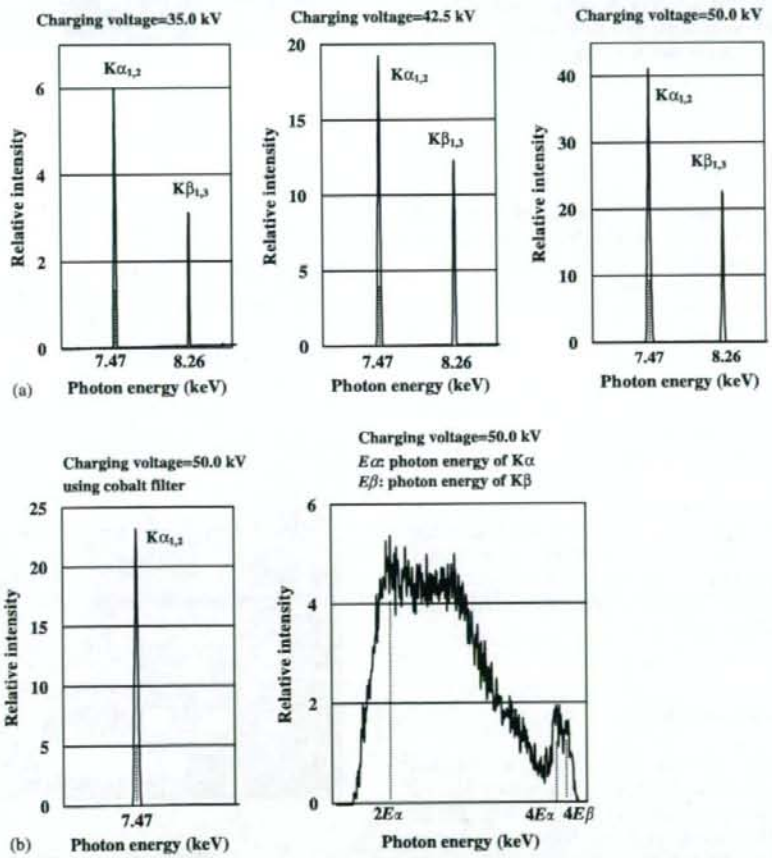

Fig. 6. X-ray spectra from weakly ionized nickel plasma at the indicated conditions. (a) Kα and Kβ rays and (b) Kα and higher harmonic rays.

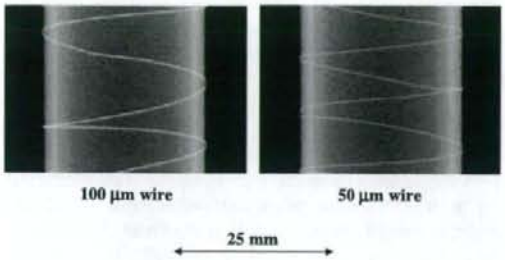

Fig. 7. Radiograms of tungsten wires coiled around PMMA pipes.

exposure time. Fig. 6 shows measured spectra from the copper target with a charging voltage of 50 kV. In fact, we observed clean K lines such as lasers, and Kα lines were left by absorbing Kβ lines using a 15-μm-thick cobalt filter. The characteristic X-ray intensity substantially increased with corresponding increases in the charging voltage, and higher harmonic hard X-rays were observed.

4. Radiography

The plasma radiography was performed by the CR system without using the filter. The charging voltage and the distance between the X-ray source and imaging plate were 50 kV and 1.2 m, respectively.

Firstly, rough measurements of spatial resolution were made using wires. Fig. 7 shows radiograms of tungsten wires coiled around pipes made of polymethyl methacrylate (PMMA). Although the image contrast decreased somewhat with decreases in the wire diameter, due to blurring of the image caused by the sampling pitch of 87.5 μm, a 50-μm-diameter wire could be observed.

Fig. 8 shows a radiogram of a vertebra, and fine structures in the vertebra were observed. Next, an image of plastic bullets falling into a polypropylene beaker from a plastic test tube is shown in Fig. 9. Because the X-ray duration was about 500 ns, the stop-motion image of bullets could be obtained.

5. Conclusions and outlook

Concerning the spectrum measurement, we obtained fairly intense and clean K lines from a weakly ionized linear plasma X-ray source, and Kα lines were left by absorbing Kβ lines using the cobalt filter. In particular, the higher harmonic X-rays were produced from the plasma. Because the X-ray intensities of the harmonics increased with increases in the charging voltage, the

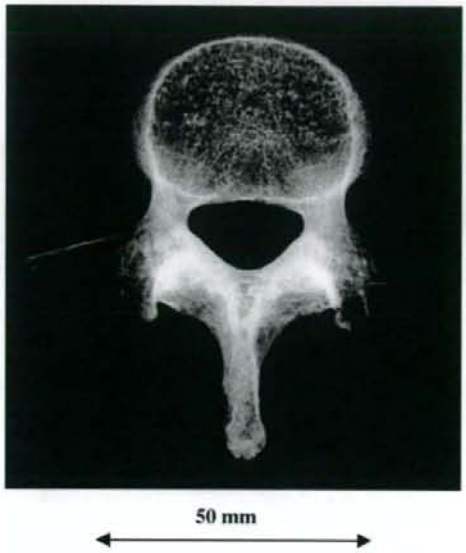

Fig. 8. Radiogram of a vertebra.

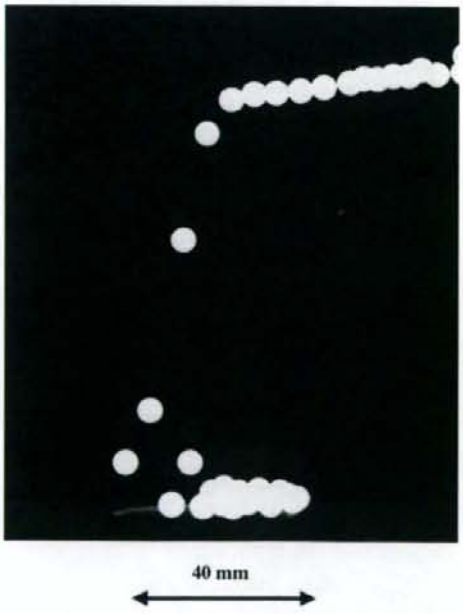

Fig. 9. Radiogram of plastic bullets falling into polypropylene beaker from a plastic test tube.

harmonic bremsstrahlung rays survived due to the X-ray resonation.

To perform monochromatic radiography, the higher harmonics are not necessary. Therefore, the condenser charging voltage should be minimized in order to decrease the intensities of higher harmonics, and the condenser capacity should be maximized to increase the characteristic X-ray intensity. On the other hand, because the intensities of harmonics increase with increases in the charging voltage, high-photon-energy monochromatic radiography may be realized.

In this research, we obtained sufficient characteristic X-ray intensity per pulse for CR radiography, and the generator produced number of characteristic K photons was approximately 1×10^8 photons/cm^2 at 1.0 m per pulse. In addition, since the photon energy of characteristic X-rays can be controlled by changing the target elements, various quasi-monochromatic high-speed radiographies, such as high-contrast angiography and mammography, will be possible.

Acknowledgments

This work was supported by Grants-in-Aid for Scientific Research (13470154, 13877114, 16591181, and 16591222) and Advanced Medical Scientific Research from MECSST, Health and Labor Sciences Research Grants (RAMT-nano-001, RHGTEFB-genome-005 and RHGTEFB-saisei-003), Grants from the Keiryo Research Foundation, the Promotion and Mutual Aid Corporation for Private Schools of Japan, the Japan Science and Technology Agency (JST), and the New Energy and Industrial Technology Development Organization (NEDO, Industrial Technology Research Grant Program in '03).

References

Ando, M., Maksimenko, M., Sugiyama, H., Pattanasiriwisawa, W., Hyodo, K., Uyama, C., 2002. A simple X-ray dark- and bright- field imaging using achromatic Laue optics. Jpn J. Appl. Phys. 41, L1016–L1018.

Davis, T.J., Gao, D., Gureyev, T.E., Stevenson, A.W., Wilkins, S.W., 1995. Phase-contrast imaging of weakly absorbing materials using hard X-rays. Nature 373, 595–597.

Germer, R., 1979. X-ray flash techniques. J. Phys. E: Sci. Instrum. 12, 336–350.

Hyodo, K., Ando, M., Oku, Y., Yamamoto, S., Takeda, T., Itai, Y., Ohtsuka, S., Sugishita, Y., Tada, J., 1998. Development of a two-dimensional imaging system for clinical applications of intravenous coronary angiography using intense synchrotron radiation produced by a multipole wiggler. J. Synchrotrón. Rad. 5, 1123–1126.

Macchietto, C.D., Benware, B.R., Rocca, J.J., 1999. Generation of millijoule-level soft-X-ray laser pulses at a 4-Hz repetition rate in a highly saturated tabletop capillary discharge amplifier. Opt. Lett. 24, 1115–1117.

Momose, A., Takeda, T., Itai, Y., Hirano, K., 1996. Phase-contrast X-ray computed tomography for observing biological soft tissues. Nat. Med. 2, 473–475.

Mori, H., Hyodo, K., Tanaka, E., Mohammed, M.U., Yamakawa, A., Shinozaki, Y., Nakazawa, H., Tanaka, Y., Sekka, T., Iwata, Y., Honda, S., Umetani, K., Ueki, H., Yokoyama, T., Tanioka, K., Kubota, M., Hosaka, H., Ishizawa, N., Ando, M., 1996. Small-vessel radiography in situ with monochromatic synchrotoron radiation. Radiology 201, 173–177.

Rocca, J.J., Shlyaptsev, V., Tomasel, F.G., Cortazar, O.D., Hartshorn, D., Chilla, J.L.A., 1994. Demonstration of a discharge pumped table-top soft X-ray laser. Phys. Lev. Lett. 73, 2192–2195.

Rocca, J.J., Clark, D.P., Chilla, J.L.A., Shlyaptsev, V.N., 1996. Energy extraction and achievement of the saturation linit in a discharge-pumped table-top soft X-ray amplifier. Phys. Lev. Lett. 77, 1476–1479.

Sato, E., Kimura, S., Kawasaki, S., Isobe, H., Takahashi, K., Tamakawa, Y., Yanagisawa, T., 1990. Repetitive flash X-ray generator utilizing a simple diode with a new type of energy-selective function. Rev. Sci. Instrum. 61, 2343–2348.

Sato, E., Takahashi, K., Sagae, M., Kimura, S., Oizumi, T., Hayasi, Y., Tamakawa, Y., Yanagisawa, T., 1994a. Sub-kilohertz flash X-ray generator utilizing a glass-enclosed cold-cathode triode. Med. Biol. Eng. Comput. 32, 289–294.

Sato, E., Sagae, M., Takahashi, K., Shikoda, A., Oizumi, T., Hayasi, Y., Tamakawa, Y., Yanagisawa, T., 1994b. 10 kHz microsecond pulsed X-ray generator utilizing a hot-cathode triode with variable durations for biomedical radiography. Med. Biol. Eng. Comput. 32, 295–301.

Sato, E., Sato, K., Tamakawa, Y., 2000. Film-less computed radiography system for high-speed imaging. Ann. Rep. Iwate Med. Univ. Sch. Lib. Arts Sci. 35, 13–23.

Sato, E., Hayasi, Y., Germer, R., Tanaka, E., Mori, H., Kawai, T., Obara, H., Ichimaru, T., Takayama, K., Ido, H., 2003a. Irradiation of intense characteristic X-rays from weakly ionized linear molybdenum plasma. Jpn J. Med. Phys. 23, 123–131.

Sato, E., Hayasi, Y., Germer, R., Tanaka, E., Mori, H., Kawai, T., Ichimaru, T., Takayama, K., Ido, H., 2003b. Quasi-monochromatic flash X-ray generator utilizing weakly ionized linear copper plasma. Rev. Sci. Instrum. 74, 5236–5240.

Sato, E., Sagae, M., Tanaka, E., Hayasi, Y., Germer, R., Mori, H., Kawai, T., Ichimaru, T., Sato, S., Takayama, Y., Ido, H., 2004a. Quasi-monochromatic flash X-ray generator utilizing a disk-cathode molybdenum tube. Jpn J. Appl. Phys. 43, 7324–7328.

Sato, E., Hayasi, Y., Germer, R., Tanaka, E., Mori, H., Kawai, T., Ichimaru, T., Sato, S., Takayama, K., Ido, H., 2004b. Sharp characteristic X-ray irradiation from weakly ionized linear plasma. J. Electron. Spectrosc. Related Phenom. 137–140, 713–720.

Sato, E., Tanaka, E., Mori, H., Kawai, T., Ichimaru, T., Sato, S., Takayama, K., Ido, H., 2004c. Demonstration of

enhanced K-edge angiography using a cerium target X-ray generator. Med. Phys. 31, 3017–3021.

Sato, E., Tanaka, E., Mori, H., Kawai, T., Ichimaru, T., Sato, S., Takayama, Y., Ido, H., 2005a. Compact monochromatic flash X-ray generator utilizing a disk-cathode molybdenum tube. Med. Phys. 32, 49–54.

Sato, E., Tanaka, E., Mori, H., Kawai, T., Sato, S., Takayama, Y., 2005b. High-speed enhanced K-edge angiography utilizing cerium plasma X-ray generator. Opt. Eng. 44, 049001–049016.

Sato, E., Tanaka, E., Mori, H., Kawai, T., Sato, S., Takayama, Y., 2005c. Clean monochromatic X-ray irradiation from weakly ionized linear copper plasma. Opt. Eng. 44, 049002–049016.

Shikoda, A., Sato, E., Sagae, M., Oizumi, T., Tamakawa, Y., Yanagisawa, T., 1994. Repetitive flash X-ray generator having a high-durability diode driven by a two-cable-type line pulser. Rev. Sci. Instrum. 65, 850–856.

Takahashi, K., Sato, E., Sagae, M., Oizumi, T., Tamakawa, Y., Yanagisawa, T., 1994. Fundamental study on a long-duration flash X-ray generator with a surface-discharge triode. Jpn J. Appl. Phys. 33, 4146–4151.

Thompson, A.C., Zeman, H.D., Brown, G.S., Morrison, J., Reiser, P., Padmanabahn, V., Ong, L., Green, S., Giacomini, J., Gordon, H., Rubenstein, E., 1992. First operation of the medical research facility at the NSLS for coronary angiography. Rev. Sci. Instrum. 63, 625–628.